ARTICLE IN PRESS

Nature Communications

https://doi.org/10.1038/s41467-026-73790-x

Article in Press

An artefact-resilient wide bandwidth bidirectional graphene neural interface

Received: 24 August 2025

Accepted: 20 May 2026

[redacted]

Cite this article as: Prokop, M., Esparza-laizzo, M., Masvidal-Codina, E. *et al.* An artefact-resilient wide bandwidth bidirectional graphene neural interface. *Nat Commun* (2026). https://doi.org/10.1038/s41467-026-73790-x

Michał Prokop, Martín Esparza-laizzo, Eduard Masvidal-Codina, Xavi Illa, Neela K. Codadu, Daman Rathore, Nicola Ria, Kostas Kostarelos, Elena del Corro, Ramon Garcia-Cortadella, Rob C. Wykes, Anton Guimerà-Brunet & Jose A. Garrido

We are providing an unedited version of this manuscript to give early access to its findings. Before final publication, the manuscript will undergo further editing. Please note there may be errors present which affect the content, and all legal disclaimers apply.

If this paper is publishing under a Transparent Peer Review model then Peer Review reports will publish with the final article.

ARTICLE IN PRESS

© The Author(s) 2026. **Open Access** This article is licensed under a Creative Commons Attribution-NonCommercial-NoDerivatives 4.0 International License, which permits any non-commercial use, sharing, distribution and reproduction in any medium or format, as long as you give appropriate credit to the original author(s) and the source, provide a link to the Creative Commons licence, and indicate if you modified the licensed material. You do not have permission under this licence to share adapted material derived from this article or parts of it. The images or other third party material in this article are included in the article's Creative Commons licence, unless indicated otherwise in a credit line to the material. If material is not included in the article's Creative Commons licence and your intended use is not permitted by statutory regulation or exceeds the permitted use, you will need to obtain permission directly from the copyright holder. To view a copy of this licence, visit http://creativecommons.org/licenses/by-nc-nd/4.0/.

An artefact-resilient wide bandwidth bidirectional graphene neural interface

Michał Prokop[1], Martín Esparza-Iaizzo[2,3], Eduard Masvidal-Codina[1,4,5], Xavi Illa[4,6], Neela K. Codadu[2], Daman Rathore[2], Nicola Ria[1], Kostas Kostarelos[1,7,5,8], Elena del Corro[1], Ramon Garcia-Cortadella[1,9], Rob C. Wykes[2,8,10], Anton Guimerà-Brunet [6,4*], Jose A. Garrido[1,7*]

1. Catalan Institute of Nanoscience and Nanotechnology (ICN2), CSIC and BIST, Campus UAB, Barcelona, Spain

2. University College London, Queen Square Institute of Neurology, London, UK

3. INBRAIN Neuroelectronics SL, Barcelona, Spain

4. Centro de Investigación Biomédica en Red de Bioingeniería, Biomateriales y Nanomedicina, Instituto de Salud Carlos III, Madrid, Spain

5. Institute of Neurosciences, UAB Medical School, Bellaterra, Spain 6. Institut de Microelectrònica de Barcelona, IMB-CNM (CSIC), Campus UAB, Bellaterra, Spain

7. Institució Catalana de Recerca i Estudis Avançats (ICREA), Barcelona, Spain

8. Centre for Nanotechnology in Medicine, Faculty of Biology Medicine & Health, AV Hill Building, University of Manchester, Manchester, United Kingdom

9. Bernstein Center for Computational Neuroscience Munich, Faculty of Medicine, Ludwig-Maximilians Universität München, Planegg-Martinsried, Munich, Germany.

10. Division of Neuroscience, School of Biological Sciences, University of Manchester, Manchester, United Kingdom

Abstract

The ability to simultaneously record and modulate neural activity is critical for next-generation bidirectional neural interfaces aiming to enable adaptive neuromodulation therapies for neurological disorders. Active graphene transistor technologies are particularly promising for neural recordings, as they extend the ability to monitor brain activity at very low frequencies and support multiplexed operation for high-density neural interfaces. However, their limited charge injection capacity makes them unsuitable for stimulation. In this work, we present a bidirectional neural interface that combines nanoporous reduced graphene oxide (rGO) microelectrodes for high charge-injection focal stimulation and graphene solution-gated field-effect transistors (gSGFETs) for brain activity monitoring. Using scalable cleanroom microfabrication techniques, we monolithically integrate these two graphene-based technologies into fully flexible neural probes, leveraging their complementary functionalities within a single-device platform. We evaluate the performance of the hybrid devices both in saline and *in vivo*, with a particular focus on transistor performance during stimulation. Our results demonstrate that the recording capability of this bidirectional neural interface, including the monitoring of infraslow and local field potential activity, is not compromised during stimulation, opening avenues for future development of adaptive infraslow-based neuromodulation therapies.

Corresponding authors: joseantonio.garrido@icn2.cat, anton.guimera@imb-cnm.csic.es

Introduction

Brain implants have proven useful in managing different neurological disorders such as Parkinson's disease (PD) [1,2,3], epilepsy [4,5], Tourette syndrome [6,7], essential tremor [8,9] and dystonia [10], among others. Most clinically available implants are unidirectional, providing electrical stimulation to neural tissue without the ability to modulate neural activity based on dynamic changes in neural signals. Implantable neural interfaces that enable bidirectional communication, can allow recording and modulation of neural activity, and offer the potential for more effective treatments. These systems can provide on-demand, patient-specific, closed-loop therapy based on detected biomarkers, which is expected to minimize side effects and extend device battery life [11,12,13,14]. A recent feasibility clinical study on PD treatment demonstrated that adaptive deep brain stimulation significantly improved motor symptoms and quality of life compared to the standard unidirectional stimulation [15].

At present, clinically approved neural implants primarily use passive metallic electrodes for both recording and stimulation. Although emerging research technologies, such as high-density microelectrode ECoG arrays [16,17,18,19,20] promise significant improvements, they also rely on passive electrodes. These devices are well suited for recording of local field potentials (LFPs) (0.5–200 Hz), high-frequency oscillations (HFOs) (200–600 Hz) and single spikes (> 1kHz). However, regardless of electrode material or performance, passive microelectrodes are limited in their ability to detect ultraslow neural signals, such as DC-shifts and infraslow activity (ISA) (<0.1 Hz). These limitations have been attributed to the instability of the electrode-electrolyte interface, electrode potential drifts, and signal attenuation caused by high electrode impedance at low frequencies [21,22].

Yet, mounting evidence indicates that infraslow electrophysiological signals can reflect core pathophysiological processes. In particular, cortical spreading depolarizations (CSDs), which are large-amplitude, slowly propagating waves of neuronal and glial depolarization [23,24,25,26], have been linked to a growing spectrum of neurological disorders, including migraine with aura [27], acute ischaemic stroke [27], traumatic brain injury [27], subarachnoid haemorrhage [27,28], glioblastoma [29,30] and epilepsy [31,32]. In patients with acute brain injury, the burden and spatial clustering of SDs correlate with secondary tissue damage and unfavourable outcomes [28,33]. Beyond CSDs, compelling evidence suggests that seizure-associated DC shifts can delineate epileptogenic cortex with higher spatial specificity than conventional band-pass filtered recordings, which integrate activity across broader neural populations [34,35].

Despite this clinical relevance, infraslow signals remain largely inaccessible in routine clinical practice. Standard clinical amplifiers are AC-coupled and deliberately suppress frequencies below ~0.1 Hz, precluding stable detection of pathological infraslow activity and DC shifts. Even when DC-coupled electrocorticography is employed in specialized centres, conventional metal electrodes suffer from signal drift, limited long-term stability, and constrained spatial sampling density [36]. As a result, the spatiotemporal dynamics of SDs and other infraslow biomarkers are often under-resolved.

Field-effect transistors (FETs) offer a fundamentally different approach: unlike passive electrodes, these active devices transduce electrophysiological activity into modulations of channel conductance enabling intrinsically DC-coupled operation [37,38]. Among the various transistor technologies that have been validated for chronic in vivo electrophysiology [39,40,41], graphene solution-gated field-effect transistors (gSGFETs) stand out due to the combination of unique graphene properties, including electrochemical inertness, high carrier mobility, biocompatibility, and flexibility [38,39,42].

Previous work has demonstrated that gSGFETs enable DC-coupled recordings and support multiplexed operation [43,44,45], positioning them as promising candidates for high-density mapping of infraslow cortical dynamics [35,39,46,47,48]. Recently, gSGFETs were shown to offer high sensitivity for detection of both ISA and high-frequency signals, mapping seizures with preictal DC shifts, SDs, and ISA for biomarker exploration [46,49].

However, while gSGFETs are particularly suited for recording, the low interfacial capacitance of single-layer graphene (typically 2 μFcm^{-2}) restricts its charge injection capacity [50] and thus limits direct stimulation. Integration with complementary stimulating electrodes is therefore required to enable wideband bidirectional communication with neural tissue. Developing such hybrid systems capable of both stable infraslow recording and controlled stimulation may open new avenues for mechanistic investigation and translational neuromodulation strategies.

To address the challenge of creating a bidirectional neural interface enabling closed-loop neuromodulation based on wideband recordings, we propose a novel device architecture that integrates gSGFETs for brain monitoring with passive reduced graphene oxide (rGO) microelectrodes for stimulation. Previous studies have highlighted the potential of rGO as a microelectrode material for high precision neural stimulation, owing to its low impedance and high charge injection [50,51,52]. The nanoporous structure of rGO, which results in a high surface-to-volume ratio, enables it to deliver stimulation at high charge density even when miniaturized to the micrometer scale and integrated into flexible microfabricated arrays [50,51,52,53].

The integration of both recording and stimulation modalities within the same device introduces several technical challenges related to the bidirectional interface performance. Stimulation pulses can interfere with sensing instrumentation by generating artefacts that can obscure the underlying neural activity [54]. These artefacts, typically being several orders of magnitude larger than the biological signals of interest, can saturate the recording electronics. Understanding and mitigating the effect of stimulation artefacts on the recorded signals is critical for developing a new generation of closed-loop systems capable of providing on-demand stimulation [54].

Here, we present a wafer-scale microfabrication process that monolithically integrates gSGFETs with rGO microelectrodes, resulting in a fully flexible, ultra-thin neural probe. We have evaluated the bidirectional capability of this technology, demonstrating that it can capture with high fidelity the high-amplitude stimulation-induced pulses without distortion. This ability facilitates the use of simple signal filtering techniques to recover brain signals below the stimulation frequency, enabling the simultaneous monitoring of low-amplitude local field potentials (LFPs) during electrical stimulation. Furthermore, we report a series of proof-of-concept *in vivo* studies using a mouse model of neocortical epilepsy that showcase the wideband recording capabilities of this bidirectional neural interface, in particular for monitoring infraslow and LFP activity to demonstrate that the recording performance is not compromised during stimulation.

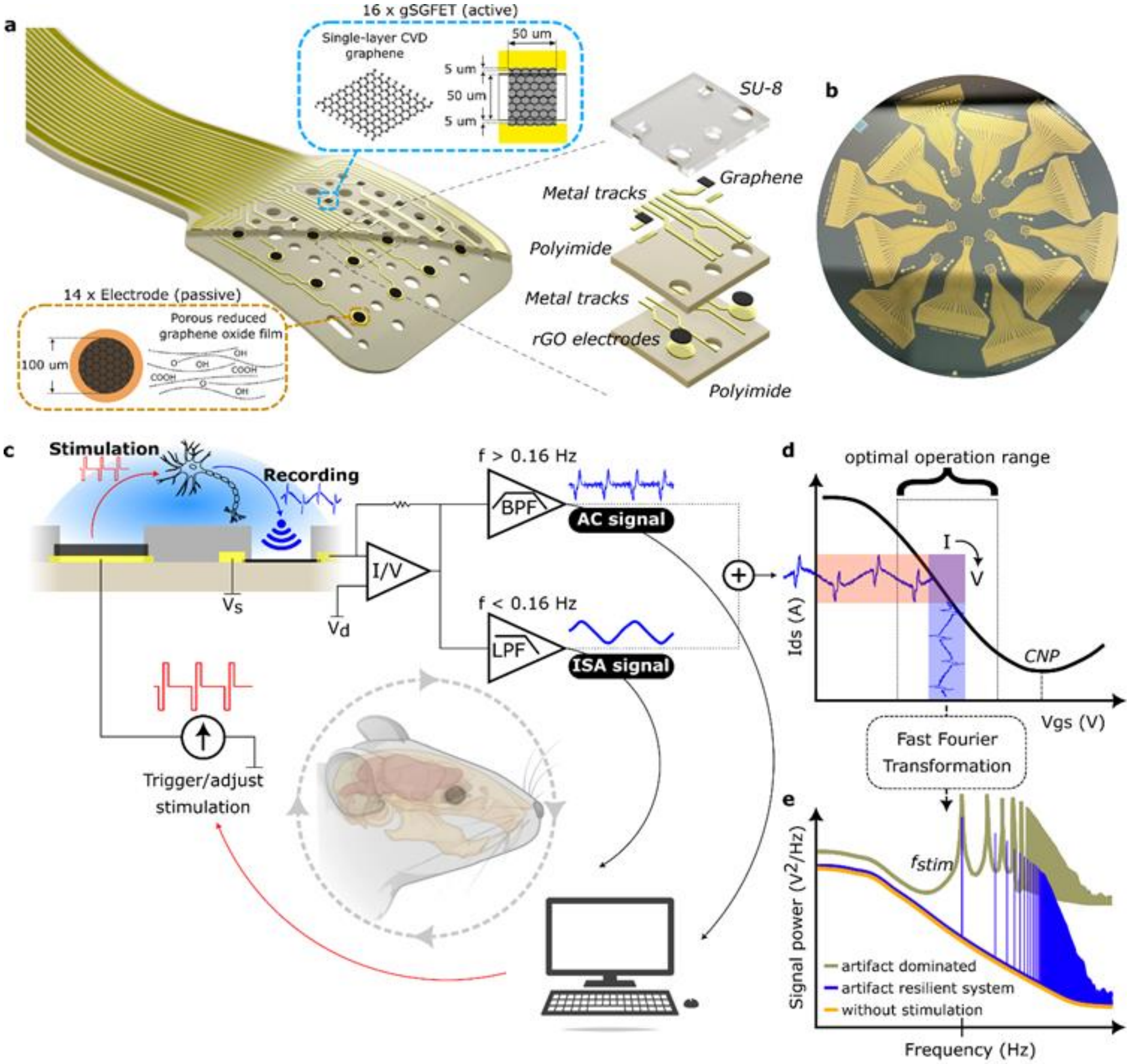

Fig. 1: An artefact-resilient wide bandwidth bidirectional graphene neural interface. a, Tip of the flexible epicortical probe containing two intermixed arrays of porous reduced graphene oxide (rGO) microelectrodes and single layer Chemical Vapor Deposition (CVD) graphene solution-gated field-effect transistors (gSGFETs). Polyimide provides insulation at the bottom and between the electrode and transistor levels while SU-8 covers the side of the probe facing tissue. **b**, Photograph of 4” wafer with 12 devices after fabrication. **c**, Closed-loop operation schematic of the active/passive hybrid device architecture. The microelectrodes enable electrical stimulation and the gSGFETs provide wide bandwidth recordings. The gSGFETs‘ ability to reliably record neural signals during simultaneous stimulation allows for precise triggering or adjustment of delivered stimulation in a closed-loop manner. To ensure proper signal acquisition across the wide range of signal amplitudes, the signal is divided into two frequency bands: the AC signal and the ISA (infraslow) signal with high and low gains, respectively. The ISA signal is defined by a low-pass filter (LPF, < 0.16 Hz) while the AC signal is defined by a band-pass filter (BPF, 0.16 - 10 kHz). Source and drain voltage are labelled as V_s and V_d. Mouse model created in BioRender, https://BioRender.com/ptmaa9o **d**, Schematic representation of gSGFET drain-source current (I_{ds}) and gate-source voltage (V_{gs}) relation. gSGFETs can to work in a wide gate voltage range, and their operation

point can be selected (by gate-source voltage, V_{gs}, adjustment in relation to the charge neutrality point, CNP), allowing them to be operated as active transducers in a wide dynamic range recording system. **e,** Power spectrum of signals acquired by artefact-dominated and artefact-resilient systems. In a recording system susceptible to stimulation artifacts, amplifier saturation can lead to contamination of the entire frequency spectrum (note the difference in stimulation frequency (f_{stim}) peak and its harmonics).

Results

Active/passive hybrid device concept for graphene-based bidirectional neural interfaces

We developed a flexible epicortical device that features two intermixed arrays: nanoporous rGO stimulating microelectrodes and gSGFETs as active sensors, all fabricated at wafer scale (Fig. 1a-b, Fig. S1). In this device, the gSGFETs provide artefact-resilient, wide-bandwidth recordings, while the rGO microelectrodes offer high charge injection capacity for stimulation. The gSGFETs' recordings can then be used to trigger or adjust the electrical stimulation delivered by the rGO microelectrodes, eventually enabling real-time, closed-loop neuromodulation (Fig. 1c).

A key technical challenge in neural implants is achieving simultaneous recording of neural activity while delivering stimulation. This is primarily due to the significant amplitude difference between neural signals and the stimulation-induced artefacts. Stimulation artefacts can reach amplitudes ranging from tens to hundreds of millivolts [55], whereas local field potentials (LFPs) are typically much smaller, often below 1 mV. Consequently, an amplification system with a large dynamic range is required to capture this range of signal amplitudes [54]. gSGFETs are well-suited for this task, as they can be operated as transducers with a very large dynamic range [37]. In a gSGFET (see Fig. 1c), the electrolyte in contact with the graphene channel functions as the gate of the transistor [37,38]. Variations in the electric potential due to neural activity couple to the channel as gate-to-source-voltage (Vgs) changes via the graphene-electrolyte interface capacitance, which alters the channel conductivity and results in drain-to-source current (Ids) changes. The Ids-Vgs curve represents the transfer function of the transducer (Fig. 1d). For gSGFETs, this transfer curve exhibits a V-shape due to the ambipolar transport in graphene, with the minimum of the curve corresponding to the charge neutrality point (CNP). Away from the CNP, the current is eventually limited by the metal-graphene contact resistance [37]. The transfer curve defines the transistor's dynamic range (Fig. 1d), typically limited to the linear part of the curve, which can be optimized by tuning the Vgs applied bias.

The transduced signal is then amplified, as described in prior works [37,38,48]. Briefly, the system consists of two stages (Fig. 1c): in the first stage, a transimpedance amplifier converts the current signal into a voltage signal. The second stage further amplifies the voltage signal before digitalization. To ensure proper signal acquisition across the wide range of signal amplitudes (from low-amplitude LFPs to large infraslow potential variations and drifts), the signal is divided into two frequency bands: the AC signal and the ISA signal (Fig. 1c) with high and low gains, respectively. The ISA signal is defined by a low-pass filter (LPF, < 0.16 Hz) while the AC signal is defined by a band-pass filter (BPF, 0.16 - 10 kHz). The total signal is then reconstructed in post-processing by summing the signals from the two bands and calibrating them through interpolation into the transistor's transfer curve, yielding distortion-free DC-coupled recordings [37].

While the above-described amplification strategy based on signal decomposition into two frequency bands is not exclusive of transistor-based systems, transistors offer several advantages that contribute to the resilience of this technology to stimulation-induced artefacts. First, the current limitation of the transistor away from the linear regime protects the transimpedance amplifier from saturation, even if the recorded signal exceeds the transistor's dynamic range. Additionally, the dynamic range of the second-stage amplifier can be fixed to match the expected range of drain-source current values, thus avoiding saturation. Second, gSGFETs can be repolarized in response to large drifts, optimizing their dynamic range. In addition, the elimination of the high-pass filter commonly employed with passive electrodes, which is necessary to enable DC-coupled recordings, facilitates rapid recovery in the unlikely event of saturation [54]. These features collectively form the basis of the high-fidelity signal recording during stimulation of this system (Fig. 1e), as demonstrated experimentally in the results presented below.

Device fabrication and characterization

The flexible epicortical design used in this study consists of two intermixed arrays of rGO microelectrodes (circular, 100 mm diameter) and gSGFETs (squared channel, 50x50 mm^2) (Fig. 2a,b). Both arrays have 4 rows and 4 columns (450 mm pitch) and are shifted by 225 mm in relation to each other. The entire array covers a total area of 1.5 mm x 1.5 mm. The fabrication begins with a sacrificial 4'' SiO_2/Si wafer substrate on which a thin layer of polyimide (PI) is deposited (Fig. 2b). Subsequently, the rGO microelectrode layer is fabricated as previously reported [50,51,52]. A second PI layer encapsulates the microelectrode layer providing electrical insulation with the transistor layer. After definition of the VIAs (vertical interconnect accesses) to electrically connect the microelectrode layer with the transistor layer, the gSGFETs are fabricated and passivated with SU-8 resist which acts as device's top encapsulation. Finally, the second PI layer is etched to expose the microelectrodes underneath. A detailed description of the fabrication protocol is provided in the Methods section and is schematically represented in Fig. 2b.

Verification of technology integration and device quality tests were conducted in a standard 1x phosphate-buffered saline (PBS) solution. The electrical characterization of the gSGFETs (see Fig. 2c-e) reveals that the performance of the gSGFETs integrated in the hybrid devices is within the expected range, in terms of transconductance and CNP, when compared with previously published data from non-hybrid devices [39,46,48]. The CNP values are homogenous within the same device and usually are only slightly offset between different microfabrication batches (Fig. 2d), which we tentatively attribute to uncontrolled doping during graphene transfer and device processing. For 160 measured transistors from various batches, the average CNP value is 0.2182 V with a standard deviation (**σ**) of 0.017 V. Similarly, the transconductance (dIds/dVgs) is also homogenous across multiple batches with a mean of 113.26 mS (**σ** <19.09 mS) for all transistors. The transistors' sensitivity has been assessed using the effective gate noise (Vrms) calculated as the root-mean-square of gate voltage noise integrated between 1Hz and 2kHz, with average values ranging between 33 and 43 mV (Fig. 2e).

The performance of microelectrodes is also homogenous across multiple devices. Electrochemical impedance characterization reveals an average impedance of 5.1 kΩ (**σ<** 0.5kΩ) at 1kHz (Fig. 2f and Fig. S2d). The maximum current that could be safely injected with the rGO microelectrodes was established by finding the biphasic pulse amplitude that elicited an electrode interfacial voltage that remains within the limits of rGO's electrochemical water window (−0.9 V for cathodic and +0.8 V for anodic versus Ag/AgCl reference) (Fig. S2e). As discussed in Supplementary Information (Fig. S3), the ohmic drop is used to calculate the interfacial voltage. Considering the maximum safe pulsed current amplitude (which we refer to as "Amax"), we characterized the voltage polarization at the electrode interface in response to biphasic pulses of varying pulse width (0.1 - 2 ms) and for a range of amplitudes (referred to 10 - 90% of Amax, typically in the range 20-390 mA, see Fig. S3c) (Fig. 2g-h). Overall, the characterization results demonstrate that the developed monolithic integration microfabrication process preserves the functional performance of both gSGFETs and rGO microelectrodes, maintaining levels comparable to those achieved when fabricated separately [46,48,52].

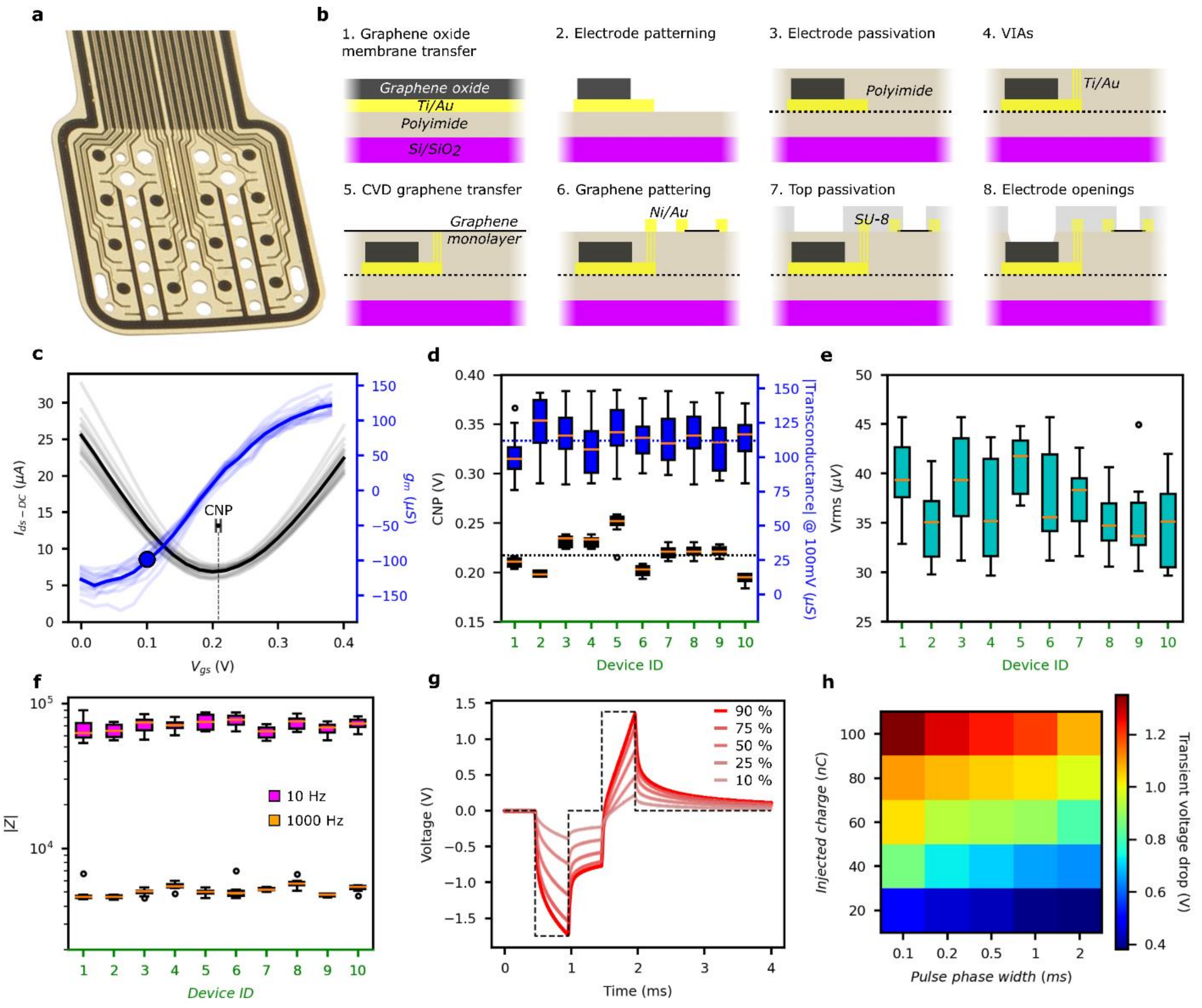

Fig. 2: Characterization of hybrid arrays. a, Photograph of the tip of a flexible epicortical probe. **b**, Microfabrication steps for the monolithic integration of the Chemical Vapor Deposition (CVD) graphene solution-gated field-effect transistors (gSGFETs) and reduced graphene oxide (rGO) microelectrodes. **c**, Individual transfer curves (drain-source current, Ids-DC, faint black lines) and transconductance (gm, faint blue lines) as a function of gate-source voltage bias (Vgs) of 16 graphene transistors in one device. Thicker lines correspond to the average of the individual transistor curves. CNP error bar shows standard deviation around mean value. **d,** Charge neutrality point (CNP) and transconductance values (for Vgs = CNP – 0.1V) dispersion statistics for 10 devices (16 transistors in each, n = 16/bar). In this figure, all boxes extend from the first quartile (Q1) to the third quartile (Q3) of the data, with a line at the median. The whiskers extend from the box to the farthest data point lying within 1.5x the inter-quartile range from the box. **e**, Transistor noise (voltage root mean square, Vrms) dispersion statistics for 10 devices (n = 16/bar). **f**, Impedance (Z) values at 10 and 1000 Hz for 10 devices (14 electrodes in each, n = 14/bar). **g**, Voltage response measured by a stimulating rGO microelectrode during application of current-controlled biphasic pulses of 500 ms (dashed lined) with increasing current amplitude; the numbers in the inset correspond to a percentage of the maximum current amplitude before the electrode is operated outside the potential window. **h**, Cathodic capacitive voltage shift measured by a rGO microelectrode during the injection of current pulses at different levels of injected charge and pulse widths.

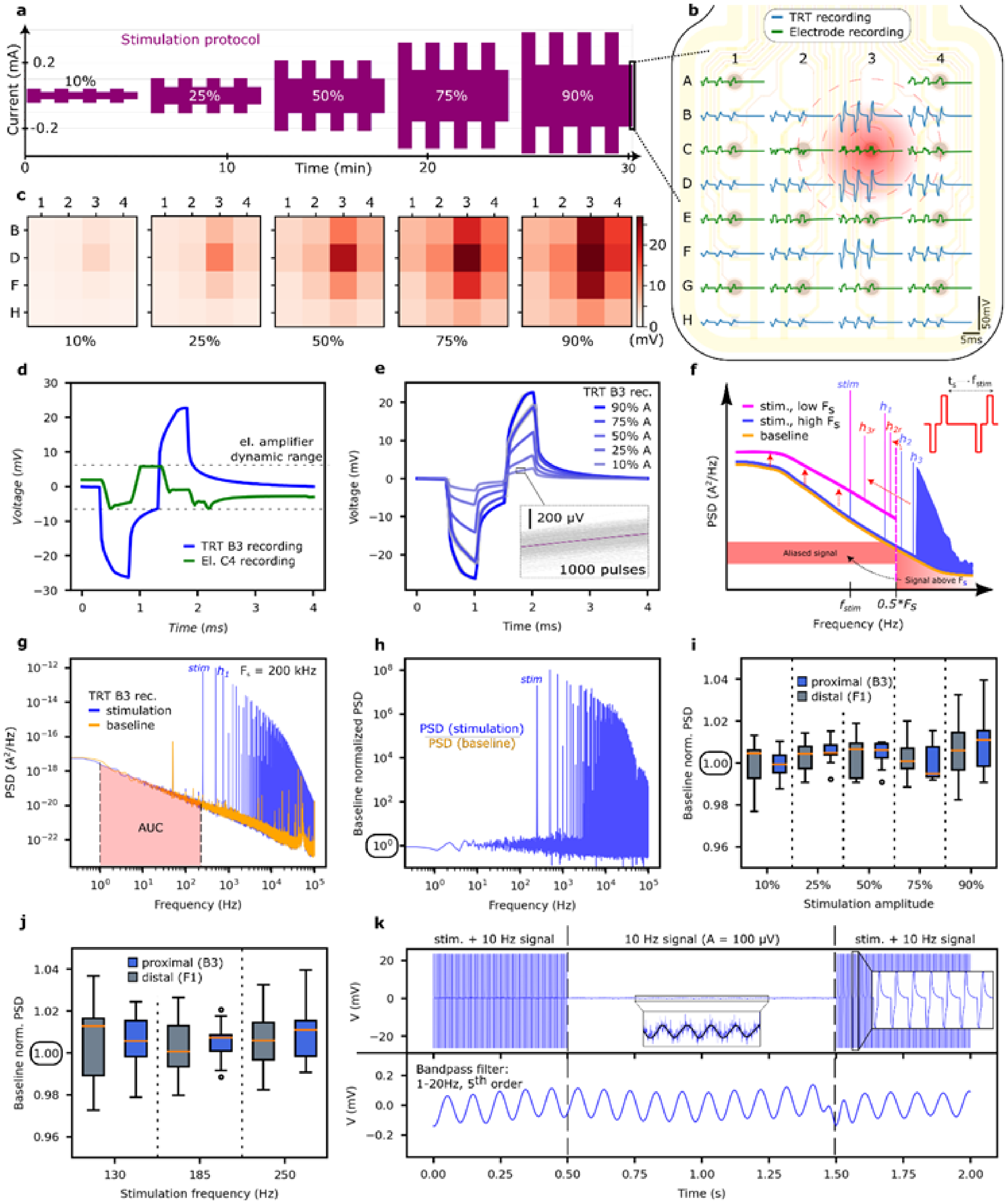

Fig. 3: In vitro assessment of recording performance of gSGFETs during stimulation. a, Stimulation protocol with combinations of various stimulation parameters: pulse width (100 or 500 ms per phase), frequency (25, 130, 185 or 250 Hz), amplitude (10, 25, 50, 75 or 90 % Amax). Each configuration lasts ~40 s. **b**, Electrode (green lines) and transistor (TRT, blue lines) recordings. Mapping of the last 3 pulses (250 Hz, 500 ms/phase, 90% Amax) in the stimulation protocol. Stimulation through electrode C3. **c**,

Stimulation induced voltage mapped by transistors. **d**, Comparison of the 500 ms stimulation-artefact pulse recorded by a transistor and an electrode, this last one showing amplifier saturation. **e**, Transistor recordings of 1000 stimulation-artefact pulses (250 Hz, 500 ms, 90% Amax); the inset shows the 1000 pulses overlapped. **f**, Schematic of noise aliasing and signal quality dependence on sampling frequency (F**s**). Stimulation causes high frequency harmonics (hi) which, due to aliasing, contaminate the frequency band of interest. Using high sampling frequency reduces the aliasing effect, as shown by the power spectral density (PSD) plot. **g**, Comparison of the PSD for the recording of a transistor in PBS with (blue) and without (orange) stimulation (250 Hz, 500 ms, 90% Amax). **h**, Ratio of the PSD values from panel g, defined as baseline-normalized PSD. **i**, Statistics of baseline-normalized PSD value as a function of the stimulation amplitude. For each amplitude, the data corresponds to the average of 9 (n = 9/bar) full stimulation protocols (as shown in panel a). In this figure, all boxes extend from the first quartile (Q1) to the third quartile (Q3) of the data, with a line at the median. The whiskers extend from the box to the farthest data point lying within 1.5x the inter-quartile range from the box. **j**, Same as in panel i, but as a function of the stimulation frequency (n = 9/bar). **k**, Raw recording and recovery of a 10 Hz signal during stimulation.

In vitro assessment of gSGFET recording performance during stimulation

The recording capabilities of gSGFETs, on the one hand, and the recording and stimulation capabilities of rGO microelectrodes, on the other hand, have been described separately in previous publications [39,43,44,45,46,47,48,50,51,52]. In this study, we evaluated the performance of monolithically integrated hybrid devices, focusing on their operation involving simultaneous stimulation and recording with the same neural probe.

Stimulation artefacts typically consist of large voltage transients resulting from the current injected through the stimulation electrode [54]. The injected current spreads through the conductive medium (tissue or electrolyte), generating a transient electric potential with an amplitude that position-dependent: higher near the stimulation electrode and decreasing away from it. When the artefact amplitude is large, it can saturate the signal acquisition chain, compromising the quality of the recorded signal.To assess the signal acquisition capability of the hybrid devices during stimulation, we designed a protocol to test a broad range of stimulation parameters we found reported in literature, including pulse width (100 or 500 ms per phase), stimulation frequency (25, 130, 185, 250 Hz), and current amplitude (10, 25, 50, 75, 90 % of Amax) (Fig. 3a). In the context of epilepsy, the vast majority of clinical studies, and all clinically approved cortical and deep brain stimulation protocols for epilepsy employ high-frequency stimulation in the range of 100–200 Hz, it is important to highlight that our device does not exhibit any inherent limitations when lower stimulation frequencies are used (Fig. S4). The stimulation protocol was applied to one electrode in the array, and the effect of the stimulation on the quality of recordings was assessed across the entire array (both for transistors and electrodes).

Fig. 3b illustrates a map of the array with representative voltage traces recorded with transistors and electrodes for a particular stimulation protocol applied to one of the electrodes (C3 in Fig. 3b). Thanks to the large dynamic range of gSGFETs, these devices can record the voltage change induced by the stimulation current pulse. As shown in Fig. 3d (see also Fig. S5 and S6 in Supplementary Information), the gSGFETs accurately measure the stimulation-induced potential change. Fig. 3e depicts voltage traces recorded by a transistor next to a stimulating electrode at various stimulation amplitudes. In this plot, the responses to 1000 consecutive stimulation pulses are superimposed, demonstrating that each stimulation pulse elicits a consistent signal as measured by the gSGFETs. In contrast, the electrodes fail to accurately capture the stimulation-induced potential changes. Under the tested stimulation conditions, the recorded signal amplitude by transistors located a few hundred micrometers from the stimulating electrode reaches tens of millivolts. As expected, the signal amplitude decreases with increasing distance from the stimulating electrode, as shown in Fig. 3c. It is important to note that the signal measured by the transistors consists of two components: an ohmic drop resulting from the injection of biphasic current pulses into the conductive medium, and a component resembling the charging behavior of a capacitor in response to the biphasic stimulation. We tentatively attribute this second component to pA-level leakage currents between the two different electronic systems dedicated to stimulation and to recording (see Figure S7 for further discussion).

Having validated the fidelity of the transistors in recording stimulation-induced pulses, we next assess the extent of stimulation-induced perturbations in the recorded signals through frequency domain analysis. Fig. 3g shows the power spectral density (PSD) of signals measured by one of the transistors with and without stimulation, using a sampling frequency of 200 kHz. Figure 3h depicts the ratio of the PSDs before and during stimulation, representing a baseline-normalized power spectral density. The PSD of the baseline signal without stimulation displays the characteristic 1/f noise of gSGFETs [39]. When stimulation is applied with a neighboring microelectrode, the PSD of the recorded signal shows a peak at the fundamental stimulation frequency (f_{stim} = 130 Hz in this case) and its corresponding harmonics. Even for the gSGFETs, high-frequency harmonics associated with the stimulation artefact, combined with the limited sampling frequency, can lead to signal contamination through aliasing. As illustrated in Figure 3f, aliasing mitigation requires careful adjustment of the antialiasing filters and selection of the sampling frequency in relation to the fundamental frequency of the stimulation pattern.

In order to quantify the level of contamination introduced by the stimulation-induced artefact in the frequency range below the stimulation frequency, we calculated the root mean square (RMS) of the recorded signal in the 1-125 Hz frequency range and computed the ratio of the RMS before and during stimulation, which could be used as indication of distortion. Figures 3i,j summarize the RMS ratio as a function of stimulation amplitude and stimulation frequency. Data were calculated based on 9 separate runs of the full stimulation protocol shown in Fig. 3a. For all tested stimulation parameters, the RMS ratio was 1 ± 0.04, indicating no significant difference between recording with and without stimulation below the stimulation frequency. Additionally, we verified that there was no difference in signal quality between recordings made by transistors that were proximal (closest to the stimulating electrode) or distal (furthest from the stimulating electrode), as shown in Fig. 3i and Fig. 3j.

As demonstrated above, in the case of the gSGFETs' recordings, the frequency range below the stimulation frequency is not altered by the artefact, which allows the use of simple frequency filtering to remove the contribution of the stimulation-induced artefact. Fig. 3k illustrates the recovery of an externally applied test signal during stimulation using only signal filtering of the raw data. In this experiment, a 10 Hz sinusoidal wave with 100 mV amplitude, simulating an LFP signal, was applied to the saline solution in which the hybrid array was tested. The top panel in Fig. 3k shows the raw data (without filtering) of the recording from one transistor during and after stimulation, while the bottom panel shows the same recording after applying a digital bandpass filter (1-20 Hz, 5th order). This experiment demonstrates that even during stimulation, when large-amplitude stimulation artefacts are present in the recordings, the gSGFETs can recover the test signal with high fidelity.

***In vivo* assessment of gSGFETs recording performance during stimulation.**

To assess the artefact resilience of the device *in vivo*, acute experiments were performed in awake head-fixed mice (n=4) (see Fig. 4a and Methods). The device was placed over the right somatosensory cortex with electrode and transistor references in the contralateral hemisphere (see Fig. 4b). The experimental paradigm consisted of a series of stimulations, each of 20 to 30 seconds of duration. 100 Hz, 21 mA (10% of Amax), 500 ms/phase biphasic pulses were applied (Fig. 4c). In order to demonstrate the ability of the gSGFETs to capture relevant biological signals we injected a chemoconvulsant (picotroxin, 10 mM) prior to electrical stimulation to induce large amplitude epileptiform activity (Fig. 4e). Following picotroxin injection, epileptic discharges developed as shown by the time series and in the frequency spectrum of an example transistor channel (see Fig. 4e). During subsequent stimulation (Fig. 4f), the frequency component of the epileptiform activity remained unaffected, as recorded by the gSGFET, showing the robustness of gSGFETs recordings to electrical stimulation artefacts in vivo. The time domain representation of the period around the stimulation (Fig. 4g) also reveals that, after low-pass filtering (<60 Hz), the recording of the epileptic activity was preserved during stimulation, in proximal as well as distal channels (colored maps in Fig. 4g).

To validate these results and determine the degree to which the signal is affected by stimulation, we quantified the effect of the artefact on the LFP band (<60Hz) employing the previously described RMS ratio (see also Fig. S8 for an *in vivo* example of the RMS ratio), which provides information about how the stimulation distorts the recorded biological signal. Fig. 4h presents the distortion factor immediately before and during stimulation across working transistors using the mapping presented in Fig. 3. Note that, although RMS ratio values are similar before and during stimulation, as well as clustered around one (i.e. no distortion), there is considerably more variance compared to the in vitro experiment (Fig. 3i,j), which we hypothesized is due to inherent variability of the biological signal. Therefore, to assess the distortion factor across all animals while accounting for the physiological changes in the biological signal, we computed the RMS ratio for each stimulation trial as well as a surrogate distribution using consecutive periods without stimulation. We then present this distribution as a kernel density estimation (KDE) which represents the variability of distortion factor values in the absence of stimulation. As shown in Fig. 4i, RMS ratio values below 60 Hz during stimulation trials fall within the limits of the surrogate distribution (gray KDE plot) and are considerably lower than the average full band RMS ratio of each trial. Altogether this demonstrates that, below the stimulation frequency, the gSGFETs present a negligible degree of distortion over baseline activity across trials and animals, enabling high-fidelity recording of the underlying relevant biological activity even during stimulation.

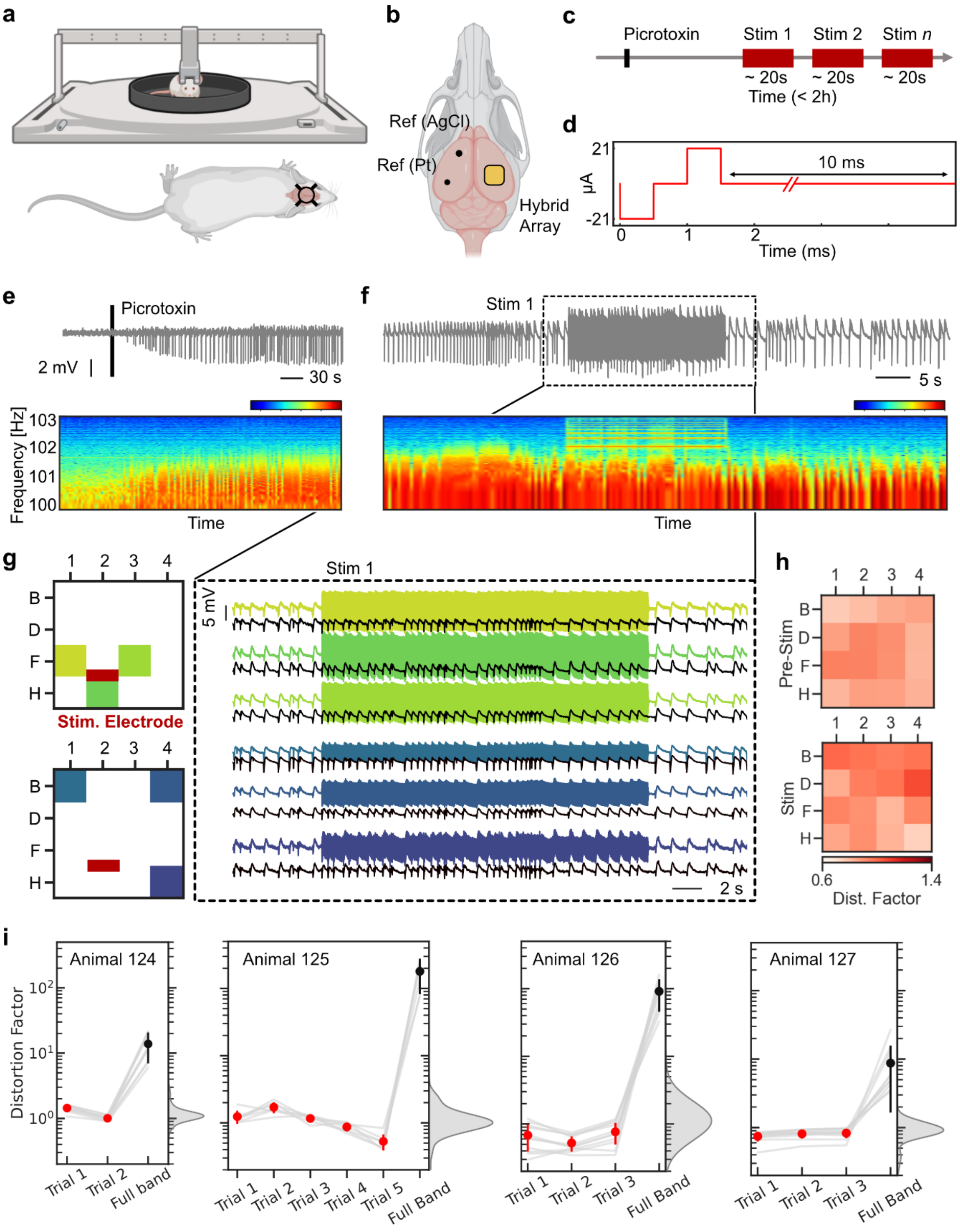

Fig. 4: *In vivo* gSGFETs recording performance during electrical microstimulation. **a**, Schematic drawing of mouse on Neurotar head-fixation system with a blow up (**b**) of the top cranial view showing the hybrid array position relative to ground and reference wires. Created in BioRender, a: https://BioRender.com/ogmyx3t, b: https://BioRender.com/ipcmyxh **c**, Experimental timeline with

indication of the picrotoxin chemo convulsant injection and subsequent stimulations. **d,** Detail of biphasic stimulation protocol. **e-f**, Voltage recording (grey) and time-frequency analysis of an example transistor channel before and after picrotoxin injection (e) and before after electrical stimulation (f). Note the limited spread of stimulation bands leaving biological activity of lower frequency unaffected. **g**, Detail of the first stimulation period across 3 proximal and 3 distal channels with full-band (colored traces) and low-pass filtered at 60 Hz activity (black traces). **h**, Spatial colormap of the RMS ratio, represented as a distortion factor, before and during stimulation for all transistor channels. **i**, RMS ratio across consecutive trials (red) of 4 animals with the averaged full band values (black) and kernel density estimate of the surrogate values in the absence of stimulation. Error bars presented as mean values with standard deviation (n = 10).

Proof-of-concept applications of the hybrid neural interface

Having established the resilience of our hybrid array to stimulation-induced artifacts in both in vitro and in vivo settings, we next evaluated its feasibility and utility for relevant biomedical applications. To this end, we conducted a series of targeted experiments to demonstrate proof of concept that the device can simultaneously deliver electrical stimulation and perform high-fidelity full-bandwidth recordings, enabling detection, induction, and modulation of infraslow brain signals, including cortical spreading depolarizations (CSDs).

CSDs are slow-moving waves of neuronal and glial depolarization implicated in a range of neurological disorders, including epilepsy, stroke, and migraine with aura [25,26,27]. The ability to detect, evoke, and eventually alter these events on demand using a single integrated platform could open new avenues in both preclinical and clinical neuroscience. Here, we first demonstrated that our hybrid array can reliably induce and record CSDs with high spatiotemporal resolution. Figure 5a shows two stimulation trains delivered via rGO microelectrodes (20 Hz, 21 μA, biphasic pulses, 5 s), and the corresponding recordings by the gSGFETs. The induced events exhibited characteristic CSD features, including a spreading wave of depolarization, suppression of high-frequency activity (Fig. S9a) with comparable amplitude and duration across animals (Fig. S9b). Electrical stimulation induced CSD events that propagated across cortical brain tissue generating heterogeneity in depolarization waveforms (Fig. S16-17). Figure 5b illustrates the timing differences in CSD onset across the transistor array, color-coded by activation time, with spatial mapping (inset) revealing earlier detection in channels closer to the stimulation site (red rectangle). A quantitative relationship between onset latency and distance to the stimulation electrode is shown in Fig. 5c ($r = 0.82$, $p = 1.9 \times 10^{-4}$). As shown in Figure S9c, the observed spatiotemporal correlation was consistent across animals and trials. These results establish that the hybrid interface can both induce and track the propagation of CSD with precision. Interestingly, in response to the 20 Hz, 5 s stimulation train, we observed localized DC shifts near the stimulating electrode that preceded CSD onset (Fig. 5d, Fig. S15), highlighting a functional advantage of the hybrid to detect pre-CSD DC shift which can be a useful biomarker of the spontaneous CSD initiation zone. These DC shifts likely reflect local accumulation of extracellular potassium released by neurons firing synchronously near the stimulation site.

We also tested the capabilities of the hybrid devices to actively steer and monitor the propagation of CSDs (Fig. 5e-h). To explore this concept, we used a previously established optogenetic model of CSD induction [47] (see Methods and Fig. S10). In the absence of electrical modulation, CSDs propagated in a repeatable manner radially from the stimulation site at an average rate of 3.66 +/- 0.33 mm/min (n=6) (Fig. 5e, Fig. S13). We attempted to modulate the propagation of CSDs through electrical stimulation applied simultaneously from 4 electrodes in a single row (Fig. 5f) and in a single column (Fig. 5g) of the hybrid device. The electrical stimulation was triggered upon CSD detection established through evaluation of the first transistor's signal slope. When electrical stimulation (150 µA, 25 Hz, 5 s from four electrodes) was applied after CSD detection, propagation was altered and accelerated toward the stimulated region (Fig. 5f-h and Fig. S13), suggesting that the hybrid interface can modulate CSD trajectory in real time. For instance, in the case of row stimulation (Fig. 5h), the CSD onset time in the B1 channel decreased to 15.1 s in comparison to 26.6 +/-2.6 s (n=6) in the control trials, showing clear acceleration effects of the stimulation in line with reported studies in ex vivo tissue [56]. Further away from the stimulation electrodes, the propagation of the CSD remains unaffected as demonstrated by very similar CSD onset delays along the top row of the array for control, horizontal and vertical stimulation experiments. For this application, we also developed a closed-loop algorithm to trigger stimulation upon SD detection (see Fig. S11 and S12) with a 0.1483 ± 0.51 s delay.

Additionally, we conducted a proof-of-concept experiment to explore how the capabilities of the device could be used to map epileptogenic tissue. In patients with drug-refractory epilepsy, surgical resection of epileptogenic tissue is sometimes possible, but only when the focus can be accurately identified. One emerging approach involves monitoring tissue responses to focal stimulation [57]. While healthy tissue typically shows time-locked evoked responses, hyperexcitable regions may generate after-discharges or seizures in response to the same stimulation [58]. To model this, we used a conditional Tuberous Sclerosis Complex 1 (TSC1) knockout mouse model of neocortical epilepsy, which exhibits spontaneous seizures and focal hyperexcitability (Fig. S14a–c). The hybrid array was positioned to span hyperexcitable and non-hyperexcitable regions. Upon stimulation, epileptiform discharges and SDs were observed only when targeting stimulation to the hyperexcitable zone (Fig. S14d), suggesting that stimulation-based mapping of epileptogenic tissue can be enhanced by simultaneous wide-bandwidth recording.

Together, these results highlight the hybrid array's ability to induce, detect, and modulate infraslow brain signals with high spatiotemporal precision, which could open new opportunities for investigating, diagnosing, and potentially treating a wide range of neurological disorders [35].

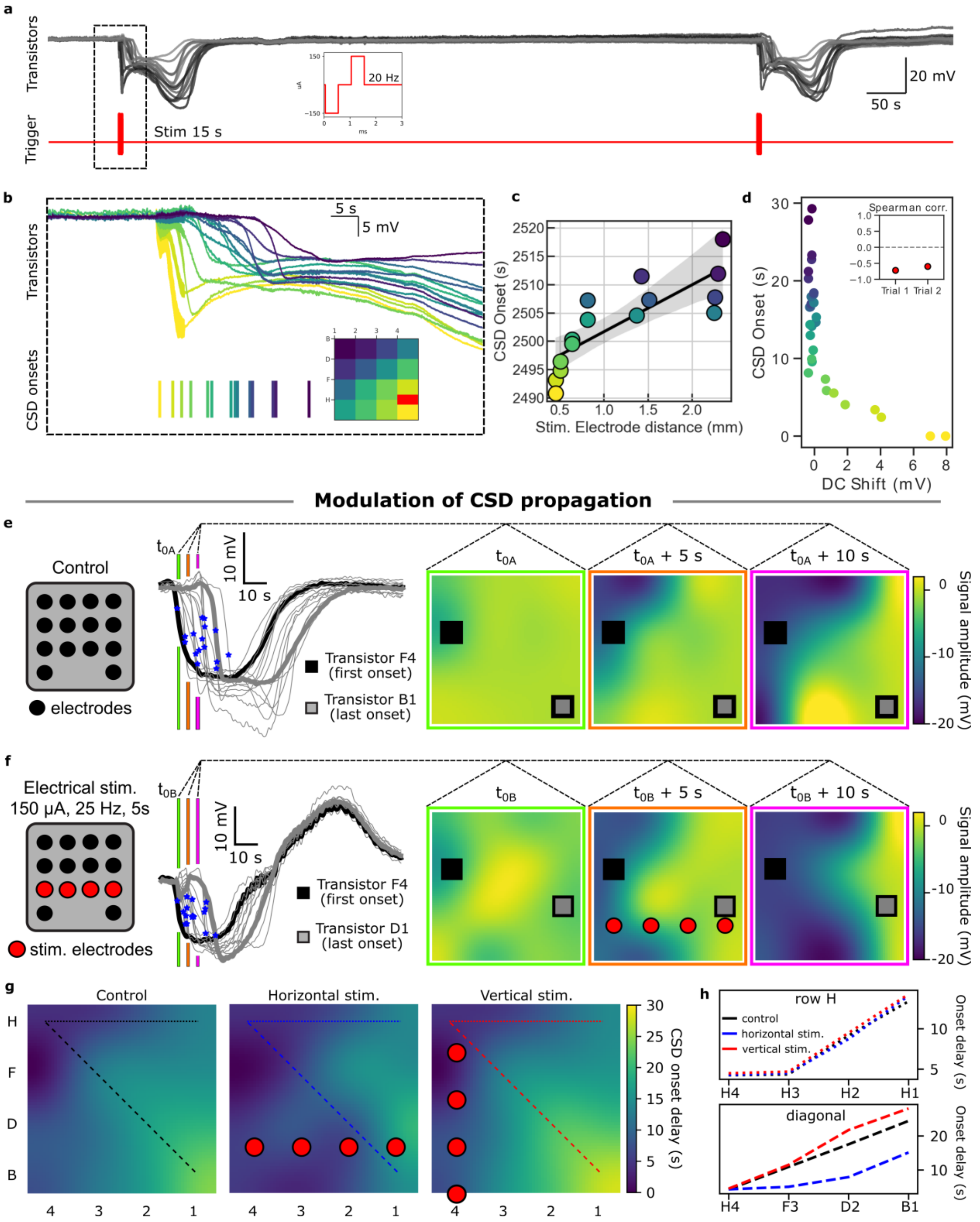

Fig. 5: Proof-of-concept applications of the hybrid neural interface. a, Reliable induction of cortical spreading depolarizations (CSDs) by electrical stimulation with microelectrodes. Inset shows stimulation train protocol of biphasic pulses at 20 Hz for 5 seconds. **b**, Detail of the initiation of the CSD (upper panel) with color-coded channels matching the beginning of the CSD. Note on the inset that the CSD originates on the lower right corner of the device, near the stimulation site (red). **c**, Linear regression between the

CSD onset of panel b and the channel distance to stimulation site. 95% confidence interval **for** the error band was used. **d**, DC shifts observed during electrical stimulation are only present in channels close to CSD onset. **e-f,** Representative examples of control spread (e) and modulation via electrical stimulation (f) of optogenetically-induced CSDs. The site of optogenetic stimulation and experimental setup is presented in Figure S10a. Stimulation protocol was triggered upon CSD detection by the first transistor (for details on CSD detection see Fig. S11). Second from the left, traces of transistor recording of a single CSD event are presented (low-pass filtered at 0.5 Hz, x-axis scale is the same for both plots in (e) and (f)). Thicker black and gray traces belong, respectively, to transistors which detected the CSD onset first (F4 in both cases) and last (B1 in (e) and D1 in (f)). CSD onsets are marked with blue stars. On the right, 3 signal amplitude maps showing CSD propagation at t_0, t_0 + 5 s and t_0 + 10 s are shown. t_0 is the time of CSD detection by the first transistor. In (f), electrical stimulation begins shortly after t_0 and finishes shortly after t_0 + 5 s. The color bars in (e) and (f) have the same scale. **g**, CSD onset delay maps showing onset times relative to the first onset detected (in all cases transistor F4) during control (no stimulation, map plotted as an average of 6 CSD events, n=6), horizontal and vertical stimulation experiments (see Fig. S13 for statistical analysis of CSD onset delays). **h,** relative onset times from (g) along the top row and diagonal of the array.

Discussion

In this work, we demonstrated the monolithic integration of passive nanoporous graphene electrodes and graphene field-effect transistors into a single device. The flexible thin-film technology was developed on 4” wafers and can be readily scaled to larger wafer sizes without significant changes. This hybrid neural interface combines the complementary advantages of passive electrodes and active transistors while preserving their respective performance, i.e. high-density microstimulation and wide-bandwidth recordings.

We validated the technology in vitro by testing a wide range of stimulation parameters, demonstrating that gSGFETs recordings are resilient to stimulation-induced artefacts allowing wide-band recordings during stimulation (Fig. S18). By achieving simultaneous recording and stimulation across a broad stimulation frequency range, our findings underscore the versatility of hybrid devices for neuromodulation applications with diverse frequency requirements.

In vivo proof-of-concept experiments further confirmed the device’s ability to induce, modulate, and monitor infraslow activity and DC shifts with high spatiotemporal precision. These capabilities extend beyond descriptive electrophysiology: they provide experimental access to infraslow dynamics that have been difficult to interrogate in a spatially resolved and bidirectional manner. As such, the hybrid platform we present in this work is not only a recording interface, but an enabling tool for mechanistic investigation of ultraslow network phenomena.

The ability to monitor SDs and DC shifts with dense spatial sampling is particularly relevant given their established role in acute brain injury and epilepsy. Because seizure-associated DC shifts and propagating depolarizations can localize pathophysiological cortex with greater specificity than conventional LFP recordings, high-resolution infraslow mapping may refine identification of epileptogenic or metabolically vulnerable regions [24,59]. More broadly, real-time detection of SD burden and propagation patterns in stroke or traumatic brain injury could provide improved biomarkers for monitoring tissue viability and informing therapeutic decision-making.

Crucially, the capacity to induce, detect, and modulate CSDs with a single device creates a framework for developing neuromodulation strategies grounded in ultraslow electrophysiology. Rather than relying on higher-frequency biomarkers, future adaptive systems may incorporate DC shifts and ISA patterns as control variables, enabling closed-loop interventions that directly target infraslow network dynamics. In epilepsy, for example, hybrid arrays could support neuromodulation strategies in which infraslow biomarkers guide stimulation paradigms. Although the hypothesis that triggered SDs might abort ongoing seizure activity [60] remains to be rigorously tested and must be evaluated in light of potential risks [61,62], our platform enables direct experimental interrogation of such mechanism under controlled conditions.

In ischaemic stroke, while CSDs initiated near the ischemic core exacerbate tissue damage [63], emerging evidence suggests that SDs arising in metabolically less compromised areas may be non-injurious or even neuroprotective [64]. By spanning the ischemic core, penumbra, and adjacent healthy cortex, the hybrid array provides a platform for spatially targeted induction and modulation of CSDs, allowing systematic evaluation of these hypotheses. Such experimental control is essential for determining whether infraslow-directed neuromodulation could be used therapeutically rather than mrerely suppressed.

Beyond acute pathologies, precise manipulation of CSDs may also inform optimization of therapeutic interventions such as electroconvulsive therapy, in which seizure-like activity and associated depolarization phenomena are induced as a part of treatment for depression [65]. We additionally demonstrate proof-of-concept steering and monitoring of CSD propagation. Although prevention of CSD propagation through stimulated areas was not achieved and comprehensive parameter optimization was beyond the scope of this study, our findings suggest that controlled modulation of CSDs using electrical fields could be possible. Localized guidance of CSDs toward regions capable of tolerating or potentially benefiting from them, and away from vulnerable regions, may represent a conceptual basis for future neuroprotective strategies [56,66,67].

While these findings represent early-stage demonstrations, they establish the technical feasibility of high-density, DC-coupled bidirectional interfaces. Thorough preclinical studies will be required to evaluate safety, efficacy, and long-term outcomes, and to define appropriate stimulation regimes for clinical translation.

In summary, this work introduces a scalable hybrid graphene neural interface that combines high-current-density microsimulation with artefact-resilient, full bandwidth recording, enabling interrogation and manipulation of brain activity across a wide electrophysiological spectrum. Our proof-of-concept studies, including spreading depolarization assessment, neuromodulation, and wide-band epileptogenic mapping, highlight the technology's potential for clinical translation. While comprehensive preclinical validation is essential to fully assess its translational viability, this technology may advance the precision and efficacy of adaptive patient-specific neuromodulation therapies.

Methods

Graphene growth

Graphene monolayers were obtained by chemical vapor deposition growth on a 4x8 cm^2 copper foils (foil thickness – 0.035 mm). The foils were electropolished in a solution containing H_2O (1 l), H_3PO_4 (0.5 l), ethanol (0.5 l), isopropanol (0.1 l) and urea (10 g) prior to the graphene growth. After polishing, the foils were placed in a quartz tube (1600 x 60 mm^2) and heated in a three-zone oven. The first annealing step at 1050 °C under a 400 sccm argon flow at 100 mbar for 1.5 h was followed by a 20 min growth step at 12 mbar under a gas mixture of 1000 sccm argon, 200 sccm hydrogen and 2 sccm of methane. The sample was then cooled under a 400 sccm argon flow by removing the quartz tube from the oven.

Graphene characterization

All graphene/Cu sheets were characterized with Raman (Witec spectrograph). 30x30 μm^2 maps were obtained with a sub-um resolution and 488 nm laser excitation wavelength to minimize copper substrate luminescence signal. The laser power was set to 1.5 mW. A 600 g/mm grating was used to provide a pixel-to-pixel spectral resolution below 3 cm^{-1}.

GO membrane preparation

Aqueous GO solution (Angstron's Materials) was diluted in deionized water to obtain a 0.15 mg/ml solution and vacuum filtered through a nitrocellulose membrane with pores of 0.025 µm, forming a thin film of GO [51]. The thin film was then transferred to the target substrate using wet transfer in deionized water and further thermal annealing at 100 °C for 2 min. The GO film–substrate stack was hydrothermally reduced at 134 °C in a standard autoclave for 3 h.

Fabrication of hybrid arrays

Hybrid arrays were fabricated using microelectronic fabrication techniques at the IMB-CNM Clean Room on sacrificial 4" Si/SiO_2 wafers. First, the wafers were cleaned in Piranha bath to remove organic contamination present on the surface. Oxygen plasma was applied to clean the surface and increase adhesion to polyimide (PI-2611, HD MicroSystems) which was then spun at 1500 rpm to form a 7,5 µm-thick layer after 350 °C bake in nitrogen atmosphere. 20 nm of Ti and 200 nm of Au were sputtered on the PI surface. Oxygen plasma was applied before GO membrane transfer, which was prepared as described above. A photolithography with an AZ nLOF 2070 (MicroChemicals) photoresist was performed to define microelectrodes followed by e-beam evaporation of 80 nm of Al and lift-off process. After the lift-off, rGO film was etched with oxygen reactive ion etching everywhere except the areas where it was protected by Al. The Al layer was then removed with standard aluminum etchant (phosphoric and nitric acid solution) revealing

100 µm diameter electrode discs. A photolithography was performed to define shapes of electrode tracks in Ti/Au metal layer. The wafers were first immersed in a commercial gold etchant solution (TechniEtch ACI2, Microchemichals) for 2 min and a mixture of propandiol:H2O:HF:50% for 1 min to etch titanium in areas not protected by the photoresist. Low power oxygen plasma was used to clean wafer surface and increase adhesion of second polyimide layer which was spun at 5000 rpm to form 2,5 µm-thick insulating film over the electrode layer. After a 350 °C bake of the PI in nitrogen atmosphere, Vertical Interconnect Accesses (VIAs) were patterned by photolithography with AZ 10xT positive resist (MicroChemicals). Oxygen reactive ion etching was used to etch through polyimide and expose electrode tracks underneath. The AZ 10xT residues were removed and photolithography with image reversal AZ 5214 resist (MicroChemicals) was done before evaporation of 10 nm of Ti and 100 nm of Au to form VIAs and first metal layer for graphene transistors located on top of the second polyimide layer over rGO electrode level. After a lift-off process, the wafer surface was treated with low power oxygen plasma to enhance adhesion with single-layer graphene (SLG) which was transferred right after using wet transfer method. Subsequently, the SLG was patterned with positive photoresist photolithography (HiPR 6512, FujiFilm) and RIE (1 min, oxygen plasma). After wafer cleaning (20 min in acetone -> 10 min in isopropanol -> 5min in DI water) another photolithography (image reversal AZ 5214 photoresist, MicroChemicals) was performed to define second metal layer for graphene transistors. Prior to evaporation of 20 nm of Ni and 200 nm of Au, 20 min of UVO treatment was applied to improve graphene/metal contacts. After the lift-off, SU-8 2005 photoresist (Kayaku Advanced Materials) was spun on the wafer at 3000 pm (2 µm-thick layer), exposed, developed and hard baked at 120 °C for 20 min. Top SU-8 passivation was followed by AZ 10xT (MicroChemicals) photolithography which defined the electrode openings. Polyimide over rGO electrodes was etched with RIE in order to create electrode openings. After wafer cleaning in isopropanol (10 min), ethanol (30 min) and DI water (5 min), the last photolithography with AZ 10xT photoresist to define device outlines and holes was done. After RIE of the two polyimide layers, the wafer was cleaned, and the flexible devices manually peeled off from the sacrificial Si/SiO_2 wafer.

Characterization of the hybrid arrays – rGO electrodes

Electrochemical characterization was performed using a potentiostat (Metrohm Autolab PGSTAT128N) in a three-electrode configuration. An Ag/AgCl electrode (FlexRef, WPI) was used as the reference electrode, and a platinum wire (Alfa Aesar, 45093) as the counter-electrode. The devices were immersed in a solution prepared by dissolving one PBS tablet (Sigma-Aldrich, P4417) in 200 ml of distilled water. The final solution contains 10 mM phosphate buffer, 137 mM NaCl, and 2.7 mM KCl at pH 7.4. Before the in vitro electrochemical evaluation, the electrodes underwent an electrochemical activation process consisting of 33 cyclic voltammetry cycles in the –0.9 V - 0.8 V range at 50 mV/s rate.

Electrochemical characterization in PBS involved measuring impedance, cyclic voltammetry, and current pulses to evaluate functionality, ensuring no broken or electrically shorted electrodes. Electrode impedance spectroscopy was conducted using the previously mentioned three-electrode setup by applying a 10 mV sinusoidal wave over a frequency range from 1 Hz to 100 kHz.

Characterization of the hybrid arrays – gSGFETs

The gSGFETS were characterized together with the electrodes in the same 150 mM PBS solution. Drain–source currents (I_{ds}) were measured varying the gate–source voltage (V_{gs}) versus a Ag/AgCl reference electrode, which was set to ground. Steady state was ensured by acquiring the current only after its time derivative was below a threshold (10^{-7} A s^{-1}). The detection limit of the gSGFET was assessed by measuring the PSD of the DC current at each polarization point V_{GS}. Integrating the PSD over the frequencies of interest (1 Hz–2 kHz) and using the transconductance allowed us to calculate V_{RMS}.

Animals

Different strains of mice were employed according to the Animal Act 1986 (United Kingdom Scientific Procedures) and under the licenses PPL PAF2788F5-13691 and PIL code 18068, endorsed by the Home Office. Animals were housed collectively as litter mates in 12 hour light/dark cycles prior to injection and head-bar surgery, after which housing was done individually. Water and food were provided throughout the day ad libitum. In vivo device performance experiments and CSD modulation experiments were carried out on wildtype (WT) C57BL/6J mice (4-6 months) while epileptogenic mapping experiments were performed using conditional TSC1-floxed mice (Jackson Laboratory) cross-bred to obtain homozygotic specimens. To obtain a focal knockout of TSC1 in astrocytes, animals were injected with a viral construct (AAV5) containing a Cre recombinase and a glial fibrillary acidic protein (GFAP) promoter. Additionally, a fluorescent tag (mCherry) was added to confirm expression (AAV5-GFAP105-mCherry-Cre, AddGene, USA). CSD modulation experiments were carried out on C57BL/6J mice injected with a viral vector (AAV9) containing ChR2 and an enhanced yellow fluorescent protein (EYFP) tag to confirm expression once again (AAV9-CamK2a-ChR2-EYFP, AddGene, USA). Selective ChR2 expression in excitatory glutamatergic neurons was achieved through a Calcium/Calmodulin Dependent Protein Kinase II Alpha (CamK2a) promoter.

Surgeries

Sterile environments and aseptic tools were common to all surgeries. Anesthesia was delivered through an isoflurane enriched chamber (1-1.5%; Henry Schein) prior to placing the animals on a stereotaxic frame (Kopf Instrumentation, USA). At the beginning of each procedure, pain relief medication was administered subcutaneously in the combined form of Meloxicam (15 mg/kg), and Buprenorphine (0.5 mg/kg). At the closure of the surgery, warmed subcutaneous saline

(0.015 ml/g) was applied at body temperature to avoid thermal shock and provide hydration. For head-plate positioning, a single hole was drilled into the skull in proximity to the left visual cortex, to support the headplate with dental cement (Kemdent, UK) and Kwik-cast (WPI, UK). Over the same surgical window, viral injections were performed in different locations for TSC1-floxed and C57BL/6J mice. In the TSC1-floxed animals, burr-holes were drilled at the following coordinates relative to bregma: ML, +2.0 mm; AP, -2.6 mm; DV, 600 µm and 350 µm. To focally knockout floxed TSC1 in astrocytes, we performed a high titer (1 x 10^{13} µg/ml) viral injection of AAV5-GFAP105-mCherry-Cre (AddGene, USA) at a rate of 75 nL/min (microinjection pump, WPI, USA). The volume at each respective depth was 400 nL and 200 nL, repeated at both sites. Delivery was achieved through a 5 µl syringe (Mo.5, Hamilton, Switzerland) in the somatosensory/visual cortex. In the CSD modulation animals, equipment remained constant, but injection sites, volumes and rates were varied. Two locations at the M2 area were selected relative to bregma: (1) ML, +0.8 mm; AP, +1.4 mm; DV, 600 µm and 350 µm, and (2) ML, +1.0 mm; AP, +2.3 mm; DV 600 µm and 350 µm. Injected volumes were 250 nL and 250 nL at each depth and site, at a rate of 50 nL/min. A high titer (1 x 10^{13} vg/ml) AAV9-CamK2a-ChR2-EYFP design was selected to express ChR2 locally. Animals were habituated in the head-fixed Neurotar system for periods of 15, 30, and 60 minutes, prior to experiments. To place the hybrid array on the brain, a craniotomy (2x2 mm) was performed on the same day of experiment over the somatosensory cortex. Additionally, to place the refences for the transistors and electrodes, we drilled two holes in the contralateral hemisphere (motor cortex for electrode reference – Pt; somatosensory for transistor reference – Ag/AgCl). Finally, in the case of CSD modulation experiments, we exposed the dura in the ipsilateral motor cortex to enable optogenetic stimulation through an optic cannula. Animals were left to recover 3-6 hours post-surgery before experiments began.

In vivo recordings

Animals were head-fixed during the experiments in the previously habituated platform and the device was positioned over the somatosensory cortex through micromanipulators. The device was connected to the corresponding hardware through a custom printed circuit board. In the CSD modulation experiments, an LED cannula (200 µm diameter, Thor Labs, USA) was positioned over the ipsilateral motor cortex. The optic stimulus was a 10-second light-on (470 nm) protocol implemented in the CLD 1015 Thor Labs controller and externally modulated from Spike2 software (version 9.16; RRID:SCR_000903). The hardware and software of the setup were similar to in vitro experiments and consisted of a series of generic and custom-built devices and programs, respectively. To acquire signals through the gSGFETs, a custom-built 16-channel amplifier (sampling frequency: 9600 Hz; g.RAPHENE, g.tec GmbH, Austria) with large dynamic range was employed. Data was visualized in real time through a Simulink model (MATLAB 2016b

RRID: SCR_001622, g.tec high speed library). To record through the glass micropipette, a Data Acquisition Unit (1401, Cambridge Electronic Design), and a 700B Multiclamp amplifier (sampling frequency: 10000 Hz) was used with Spike2 software. Electric stimulation was configured in MC_stimulus II (version 3.5.11) and delivered by the MCS stimulus generator STG4008 (8-channel) and STG4002 (2-channel; Multichannel Systems, Harvard Bioscience Inc.). A subset of experiments was carried out with the RHS Stim/Recording Controller (Intan Technologies) and 16-channel RHS Intan head stages.

Closed-loop algorithm for detection and modulation of Cortical Spreading Depolarizations

The implemented in Simulink algorithm uses gSGFET signal (full band or just the infraslow part, <0.16 Hz) derivative calculated in real time. The stimulation is triggered when the derivative exceeds a previously defined threshold (Fig. S11a). The threshold was established based on our previous CSD studies [47,49]. Any gSGFET can be used for detection allowing for dynamic adjustment of the set of electrodes delivering stimulation based on CSD location. Across 10 trials, the computed delay between CSD detection and stimulation initiation (see Fig. S11c) amounted to 0.1483 ± 0.51 s (mean ± standard error of the mean). This relatively high value comes from the slowness of communication with the equipment used for stimulation and could be significantly reduced if an equipment with faster interface was used. Nevertheless, this delay is negligible in this application since CSD propagation is orders of magnitude slower, ~4 mm/minute. The details about software implementation of the closed-loop algorithm in the Simulink environment are presented in Figure S12.

Ethics

Every experiment involving animals, human participants, or clinical samples has been carried out following a protocol approved by an ethical commission.

Data analysis

Electrophysiological signals recorded in vivo were processed using Python packages including Numpy 1.21.5, Neo 0.11.1, pandas, seaborn 0.11.2, Matplotlib 3.5.1, Quantities 0.13.0, Elephant 0.10.0, and the custom library PhyREC 0.6.5.

Data presented in panels e-h in Fig. 5 was prepared in the following way. Transistor recordings were calibrated using transistor characterization curves measured before the experiment and subsequently downsampled to 1200 Hz. To remove channel offsets, a constant value for each channel (this constant was calculated as an average of 10000 data points of an uneventful part of each recording a few seconds before each CSD event) was subtracted from every data point. Two broken channels (in positions H4 and D2) were interpolated by averaging signals from neighboring channels). Low pass filter at 0.5 Hz was applied to each channel. CSD onsets were calculated for each channel by calculating signal derivative and finding its minimum in the range of CSD initiation. CSD onsets for all channels were normalized with respect to the channel with the lowest onset (t = 0) by subtracting the lowest channel offset from all offsets.

Data Availability

All the main text data used in this study is available here: https://doi.org/10.34810/data2776. All data supporting the findings of this study are available within the article and its supplementary files. Any additional requests for information can be directed to, and will be fulfilled by, the corresponding authors. Source data are provided with this paper.

Code availability

Custom code developed for neurophysiological analysis is available at https://github.com/aguimera/PhyREC. Custom scripts can be found at https://doi.org/10.34810/data2776 and freely used under MIT license.

References

1. Starr, P.A. Totally Implantable Bidirectional Neural Prostheses: A Flexible Platform for Innovation in Neuromodulation. *Front. Neurosci.* **12**, 619 (2018).
2. Arlotti, M. et al. A New Implantable Closed-Loop Clinical Neural Interface: First Application in Parkinson's Disease. *Front. Neurosci.* **15**, 763235 (2021).
3. Little, S. et al. Bilateral adaptive deep brain stimulation is effective in Parkinson's disease. *Journal of Neurology, Neurosurgery & Psychiatry* **87,** 717-721 (2016).
4. Anderson, D.N. et al. Closed-loop stimulation in periods with less epileptiform activity drives improved epilepsy outcomes. *Brain*, **147**, 521–531 (2024).

5. Nair, D.R. et al. Nine-Year Prospective Efficacy and Safety of Brain-Responsive Neurostimulation for Focal Epilepsy. *Neurology* **95**, e1244–e1256 (2020).
6. Molina, R. et al. Report of a patient undergoing chronic responsive deep brain stimulation for Tourette syndrome: proof of concept. *J. Neurosurg*. **129**, 308-314 (2018).
7. Marceglia, S. et al. Adaptive Deep Brain Stimulation (aDBS) for Tourette Syndrome. *Brain Sci.* **8**, 4 (2017).
8. Opri, E. et al. Chronic embedded cortico-thalamic closed-loop deep brain stimulation for the treatment of essential tremor. *Sci. Transl. Med.* **12**, eaay7680 (2020).
9. He, S. et al. Closed-loop DBS triggered by real-time movement and tremor decoding based on thalamic LFPs for essential tremor. *Annu. Int. Conf. IEEE Eng. Med. Biol. Soc.* 3602-3605 (2020).
10. Johnson, V. et al. Embedded adaptive deep brain stimulation for cervical dystonia controlled by motor cortex theta oscillations. *Experimental Neurology* **345**, 113825 (2021).
11. Schultz, D.M. et al. Sensor-driven position-adaptive spinal cord stimulation for chronic pain. *Pain Physician* **15**, 1–12 (2012).
12. Little, S. et al. Adaptive deep brain stimulation in advanced Parkinson disease. *Ann Neurol.* **74**, 449–457 (2013).
13. Sun, F.T., Morrell, M.J. Closed-loop neurostimulation: the clinical experience. *Neurotherapeutics* **11**, 553-63 (2014).
14. Rosin, B. et al. Closed-loop deep brain stimulation is superior in ameliorating parkinsonism. *Neuron* **72**, 370–384 (2011).
15. Oehrn, C.R. et al. Chronic adaptive deep brain stimulation versus conventional stimulation in Parkinson's disease: a blinded randomized feasibility trial. *Nat. Med.* **30**, 3345–3356 (2024).
16. Barth, K.J. et al. Flexible, high-resolution cortical arrays with large coverage capture microscale high-frequency oscillations in patients with epilepsy. *Epilepsia* **64**, (7):1910-1924 (2023).
17. Hettick, M. et al. Minimally invasive implantation of scalable high-density cortical microelectrode arrays for multimodal neural decoding and stimulation. *Nat. Biomed. Eng.* (2025). https://doi.org/10.1038/s41551-025-01501-w
18. Hu, J. et al. Fully desktop fabricated flexible graphene electrocorticography (ECoG) arrays. *J. Neural Eng.* **18**, 20(1):10.1088/1741-2552/acae08 (2023).
19. Setogawa, S. et al. A novel micro-ECoG recording method for recording multisensory neural activity from the parietal to temporal cortices in mice. *Mol. Brain.* **16**, 38 (2023).
20. Jeong, U.J. et al. A minimally invasive flexible electrode array for simultaneous recording of ECoG signals from multiple brain regions. *Lab Chip* **15**, 21(12):2383-2397 (2021).
21. Nelson, M.J., Pouget, P., Nilsen, E.A., Patten, C.D., Schall, J.D. Review of signal distortion through metal microelectrode recording circuits and filters. *J. Neurosci. Methods* **30**, 141-57 (2008).
22. Chunyan, L. et al. Evaluation of microelectrode materials for direct-current electrocorticography. *J. Neural Eng.* **13**, 016008 (2016).

23. Mitra, A. et al. Spontaneous Infra-slow Brain Activity Has Unique Spatiotemporal Dynamics and Laminar Structure. *Neuron* **98**, 297-305.e6 (2018).
24. Lee, S. et al. DC shifts, high frequency oscillations, ripples and fast ripples in relation to the seizure onset zone. *Seizure* **77**, 52-58 (2020).
25. Pietrobon, D., Moskowitz, M.A. Chaos and commotion in the wake of cortical spreading depression and spreading depolarizations. *Nat. Rev. Neurosci.* **15**, 379-93, (2014).
26. Leao, A.A.P. Spreading depression of activity in the cerebral cortex. *Journal of Neurophysiology* **7**, 359-390 (1944).
27. Lauritzen, M. et al. Clinical relevance of cortical spreading depression in neurological disorders: migraine, malignant stroke, subarachnoid and intracranial hemorrhage, and traumatic brain injury. *J Cereb. Blood Flow Metab.* **31**, 17-35 (2011).
28. Dreier, J.P. et al. Delayed ischaemic neurological deficits after subarachnoid haemorrhage are associated with clusters of spreading depolarizations. *Brain* **129**, 3224-37 (2006).
29. Curry, R.N. et al. Glioma epileptiform activity and progression are driven by IGSF3-mediated potassium dysregulation. *Neuron* **111**, 682-695.e9 (2023).
30. Hills, K.E., Kostarelos, K., Wykes, R.C. Converging Mechanisms of Epileptogenesis and Their Insight in Glioblastoma. *Front. Mol. Neurosci.* **15**, 903115 (2022).
31. Aiba, I. Heterogeneous Mechanisms of Spreading Depolarization and Seizures. In*:* Noebels, J.L., Avoli, M., Rogawski, M.A., Vezzani, A., Delgado-Escueta, A.V, editors. *Jasper's Basic Mechanisms of the Epilepsies.* 5th ed. New York: Oxford University Press, ch. 62 (2024).
32. Dreier, J.P. et al. Spreading convulsions, spreading depolarization and epileptogenesis in human cerebral cortex. *Brain* **135**, 259-75 (2012).
33. Fabricius, M. et al. Cortical spreading depression and peri-infarct depolarization in acutely injured human cerebral cortex. *Brain* **129**, 778-90 (2006).
34. Kanazawa, K. et al. Intracranially recorded ictal direct current shifts may precede high frequency oscillations in human epilepsy. *Clinical Neurophysiology* **126**, 47-59 (2014).
35. Wykes, R.C., Masvidal-Codina, E., Guimerà-Brunet, A., Garrido, J.A. The advantages of mapping slow brain potentials using DC-coupled graphene micro-transistors: Clinical and translational applications. *Clin. Transl. Med*. **12**, 7:e968 (2022).
36. Dreier, J.P. et al. Recording, analysis, and interpretation of spreading depolarizations in neurointensive care: Review and recommendations of the COSBID research group. *J. Cereb. Blood Flow Metab.* **37**, 1595-1625 (2017).
37. Garcia-Cortadella, R. et al. Distortion-Free Sensing of Neural Activity Using Graphene Transistors. *Small* **16**, 1906640 (2020).
38. Hebert, C. et al. Flexible Graphene Solution-Gated Field-Effect Transistors: Efficient Transducers for Micro-Electrocorticography. *Advanced Functional Materials* **28**, 1703976 (2017).
39. Garcia-Cortadella, R. et al. Graphene active sensor arrays for long-term and wireless mapping of wide frequency band epicortical brain activity. *Nat. Commun.* **12**, 211 (2021).
40. Viventi, J. et al. Flexible, foldable, actively multiplexed, high-density electrode array for mapping brain activity *in vivo*. *Nat. Neurosci.* **14**, 1599–1605 (2011).

41. Khodagholy, D. et al. *In vivo* recordings of brain activity using organic transistors. *Nat. Commun.* **4**, 1575 (2013).
42. Hess, L.H., Seifert, M., Garrido, J.A. Graphene Transistors for Bioelectronics. *Proceedings of the IEEE* **101**, 1780-1792 (2013).
43. Cisneros-Fernández, J. et al. A 1024-Channel 10-Bit 36-µW/ch CMOS ROIC for Multiplexed GFET-Only Sensor Arrays in Brain Mapping. *IEEE Transactions on Biomedical Circuits and Systems* **15**, 860-876 (2021).
44. Garcia-Cortadella, R. et al. Switchless Multiplexing of Graphene Active Sensor Arrays for Brain Mapping. *Nano Letters* **20**, 3528-3537 (2020).
45. Schaefer, N. et al. Multiplexed neural sensor array of graphene solution-gated field-effect transistors. *2D Mater.* **7**, 025046 (2020).
46. Bonaccini Calia, A. et al Full-bandwidth electrophysiology of seizures and epileptiform activity enabled by flexible graphene microtransistor depth neural probes. *Nat. Nanotechnol.* **17**, 301–309 (2022).
47. Masvidal-Codina, E. et al. Characterization of optogenetically-induced cortical spreading depression in awake mice using graphene micro-transistor arrays. *J. Neural Eng.* **18**, 055002 (2021).
48. Masvidal-Codina, E. et al. High-resolution mapping of infraslow cortical brain activity enabled by graphene microtransistors. *Nature Mater.* **18**, 280–288 (2019).
49. Flaherty, S. et al. Graphene Micro-transistor Arrays Reveal Perfusion-Dependent Electrophysiological and Haemodynamic Signatures of Cortical Spreading Depolarizations in Ischaemic Stroke. bioRxiv 2025.05.15.654197; doi: https://doi.org/10.1101/2025.05.15.654197 (2025).
50. Ria, N. et al. Flexible graphene-based neurotechnology for high-precision deep brain mapping and neuromodulation in Parkinsonian rats. *Nature Communications* **16**, 2891 (2025).
51. Viana, D. et al. Nanoporous graphene-based thin-film microelectrodes for in vivo high-resolution neural recording and stimulation. *Nat. Nanotechnol.* **19**, 514–523 (2024).
52. Duvan, F.T. et al. Graphene-based microelectrodes with bidirectional functionality for next-generation retinal electronic interfaces. *Nanoscale Horiz.* **9**, 1948-1961 (2024).
53. Bernicola, M.P., et al. The impact of graphene oxide nanosheet lateral dimensions on the electrochemical performance of nanoporous graphene-based electrodes. *Diamond and Related Materials* **150**, 111722 (2024).
54. Zhou, A., Johnson, B.C., Muller, R. Toward true closed-loop neuromodulation: artifact-free recording during stimulation. *Curr. Opin. Neurobiol.* **50**, 119-127 (2018).
55. Ramasubbu, R., Lang, S., Kiss, Z.H.T. Dosing of Electrical Parameters in Deep Brain Stimulation (DBS) for Intractable Depression: A Review of Clinical Studies. *Front. Psychiatry* **11**, 302 (2018).
56. Whalen, A.J. et al. Control of Spreading Depression with Electrical Fields. *Sci. Rep.* **8**, 8769 (2018).

57. Valentín, A. et al. Responses to single pulse electrical stimulation identify epileptogenesis in the human brain in vivo. *Brain* **125**, 1709-1718 (2002).
58. Trébuchon, A., Chauvel, P. Electrical Stimulation for Seizure Induction and Functional Mapping in Stereoelectroencephalography. *J. Clin. Neurophysiol*. **33**, 511-521 (2016).
59. Ikeda, A. et al. Active direct current (DC) shifts and "Red slow": two new concepts for seizure mechanisms and identification of the epileptogenic zone. *Neuroscience Research*, **156**, 95-101 (2020).
60. Norby, J.H. et al. Rodent and human seizures demonstrate a dynamic interplay with spreading depolarizations. *Neurobiol Dis.* **211**, 106937 (2025).
61. Aiba, I., Noebels, J.L. Spreading depolarization in the brainstem mediates sudden cardiorespiratory arrest in mouse SUDEP models. *Sci. Transl. Med.* **7**, 282:282ra46 (2015).
62. Jansen, N.A. et al. Apnea Associated with Brainstem Seizures in *Cacna1a*^{S218L} Mice Is Caused by Medullary Spreading Depolarization. *J Neurosci.* **39**, 48:9633-9644 (2019).
63. Dreier, J. The role of spreading depression, spreading depolarization and spreading ischemia in neurological disease. *Nat Med* **17**, 439–447 (2011).
64. Sugimoto, K. et al. Optogenetic Spreading Depolarizations Do Not Worsen Acute Ischemic Stroke Outcome. *Stroke* **54**, 4 (2023).
65. Rosenthal, Z.P., Majeski, J.B., Somarowthu, A. et al. Electroconvulsive therapy generates a postictal wave of spreading depolarization in mice and humans. *Nat Commun* **16**, 4619 (2025).
66. Koroleva, V.I., Bures, J. Circulation of cortical spreading depression around electrically stimulated areas and epileptic foci in the neocortex of rats. *Brain Research* **173**, 2:209-215 (1979).
67. Koroleva, V.I., Bures, J. Blockade of cortical spreading depression in electrically and chemically stimulated areas of cerebral cortex in rats. *Electroencephalography and Clinical Neurophysiology* **48**, 1:1-15 (1980).

Funding

This research was funded by the European Union's Horizon 2020 research and innovation programme under grant agreement no. 881603 (Graphene Flagship Core 3) and the European Union's Horizon Europe research and innovation programme under grant agreement 101070865 (MINIGRAPH) and 101130650 (META-BRAIN). The ICN2 has been supported by the Severo Ochoa Centres of Excellence programme [SEV-2017-0706]. ICN2 and IMB-CNM are currently supported by the Severo Ochoa Centres of Excellence and Maria de Maeztu Units of Excellence programme, grant CEX2021-001214-S and grant CEX2023- 001397-M, respectively, both funded by MCIN and MCIU/AEI/10.13039.501100011033. ICN2 is also supported by the CERCA Programme of Generalitat de Catalunya. This research is also funded by the Spanish Ministerio de Ciencia e Innovación (PID2020-113663RB-I00 and PID2021-126117NA-I00) founded by MCIU/AEI/10.13039/ 501100011033) and by "ERDF A way of making Europe", PLEC2022-009232, PCI2021-122095-2A and CNS2023-144492, funded by MCIU/AEI /10.13039/501100011033 and the European Union Next-GenerationEU/PRTR. N. R. acknowledges grant PRE2020-093708 founded by MCIN/AEI /10.13039/501100011033 and by FSE. E. M. C. acknowledges grant FJC2021-046601-I funded by Agencia Estatal de Investigacion of Spain and the European Union Next-GenerationEU/PRTR. This work has made use of the Spanish ICTS Network MICRONANOFABS, partially supported by MICINN and the ICTS NANBIOSIS, specifically by the Micro-NanoTechnology Unit U8 of the CIBER-BBN. This research was supported by CIBER - Consorcio Centro de Investigación Biomédica en Red- (CB06/01/0049), Instituto de Salud Carlos III, Ministerio de Ciencia e Innovación. The project that gave rise to these results received the support of a fellowship from the "la Caixa" Foundation (ID 100010434). M. P. acknowledges grant with fellowship code LCF/BQ/DI21/11860021.

Contributions

M. P. worked on the design, fabrication, characterization and development of the devices; worked on the *in vivo* experimental design, data collection, and analysis of the *in vitro* data and *in vivo* data; worked on the preparation of figures and writing of the manuscript, participated in and contributed to the in vivo experiments.

M. E.-I. worked on the *in vivo* experimental design, data collection, and analysis; contributed to animal handling; carried out histological sectioning and imaging; preparation figures and writing of the manuscript.

E. M.-C contributed to the characterization of the devices, data analysis, and manuscript preparation.

X. I. and N. R. contributed to the fabrication process.

N. C. and D. R. carried out animal surgeries, habituations, and in *vivo* experiments.

K. K., E. C. and R. G.-C contributed to the manuscript preparation.

R. W., A. G.-B. and J. A. G. designed and supervised the project and contributed to the manuscript preparation.

Competing interests

M.E-I., A.G.B., K.K., and J.A.G. declare that they hold interest in INBRAIN Neuroelectronics which has licensed the electrode technology described in this paper. All other authors declare no competing interests.

Editor's Summary

Recording and modulating neural activity is critical for next-generation bidirectional neural interfaces. Here the authors present a bidirectional neural interface based on graphene transistors, to artefact-resilient and full frequency bandwidth

Peer Review Information: *Nature Communications* thanks Sungchil Yang, and the other, anonymous, reviewer(s) for their contribution to the peer review of this work. A peer review file is available.